

## Asymmetry in Three-Site Relaxation-Exchange NMR

Bernhard Blümich,<sup>1</sup> Matthew Parziale,<sup>2</sup> and Matthew Augustine<sup>2</sup>

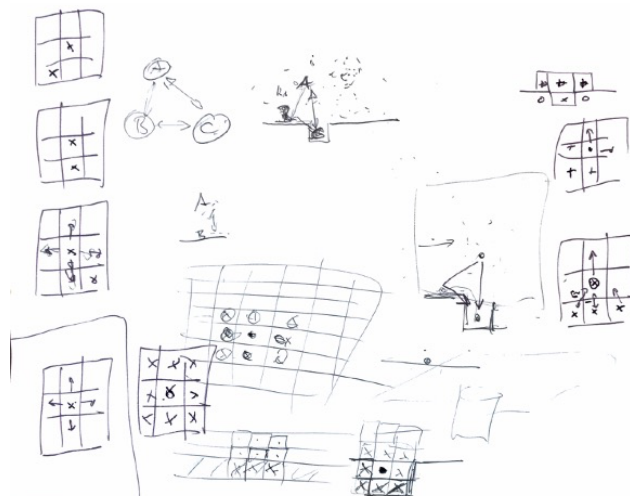
<sup>1</sup> Institut für Technische und Makromolekulare Chemie, RWTH Aachen University,  
Worringer Weg 2, 52074 Aachen, Germany

<sup>2</sup> Department of Chemistry, UC Davis, One Shields Avenue, Davis, CA 95616, USA

Corresponding author: Bernhard Blümich, [bluemich@itmc.rwth-aachen.de](mailto:bluemich@itmc.rwth-aachen.de)

10 Asymmetry of peak integrals in 2D relaxation maps of exchange between three sites  
11 reports circular flow between the relaxation sites. This disagrees with detailed balance  
12 according to which the exchange between any pair of sites must be balanced in  
13 thermodynamic equilibrium. Confined diffusion of particles jumping randomly on a 2D  
14 checkerboard grid to any of their eight neighbor positions and confined gas diffusion  
15 were modelled in Monte Carlo simulations to explore the impact of topological  
16 constraints on particle exchange between three pools. Both models produce density  
17 variations across the pore and reveal that up to 1% of the molecules move in circular  
18 paths between the relaxation pools. This motion is driven by different features of either  
19 algorithm. It is silent in thermodynamic equilibrium, confirming that multisite exchange  
20 maps are symmetric in this case. The coherent flux is argued to result from stochastic  
21 pore resonance related to diffusion eigenmodes. If it can be driven experimentally by  
22 external time-varying electric, magnetic or ultrasonic fields, this may be a way to  
23 enhance heterogeneous catalysis.

24



25

26 Graphical abstract: Draft of particle exchange on a 2D checkerboard grid

## 1. Introduction

Exchange is an essential ingredient of diffusion and spreading phenomena, which are abundant in nature and govern the evolution of tangible and intangible objects and goods (Bunde et al., 2018) as well as the physics of living systems (Gnesotto et al., 2018; Lynn et al., 2021). Nuclear Magnetic Resonance provides particularly powerful methodologies to investigate molecular exchange processes (Ernst et al., 1987; Callaghan, 2011). Slow molecular exchange on the millisecond time scale is studied by e. g. two-dimensional exchange NMR, i. e. by chemical exchange spectroscopy for rotational motion (Jeener et al., 1979) and by exchange relaxometry for translational motion (Lee et al., 1993). In equilibrium the nature of the exchange processes is commonly understood to be random Brownian motion, and the associated 2D NMR exchange maps are expected to be symmetric with respect to their diagonal. On the other hand, exchange in non-equilibrium leads to asymmetry. This has been observed in NMR, for example, in 2D chemical exchange spectra for chemical reactions involving different sites (Lacabanne et al., 2022), for the spread of hyperpolarization by spin diffusion (Björgvinsdóttir et al., 2021), for slow flow across porous media in relaxation exchange maps (Olaru et al., 2012), as well as in position- and velocity-exchange NMR (Han and Blümich, 2000).

The kinetics of transitions or exchange between discrete states driven by random processes are described by (van Kampen, 1992)

$$\frac{dM_i(t)}{dt} = \sum_j \{k_{ij}M_j(t) - k_{ji}M_i(t)\}, \quad (1)$$

where  $M_i$  are populations represented in NMR by magnetization components collected in the vector  $\mathbf{M}$ , and  $k_{ij}$  are the exchange rates equivalent to the transition probabilities from state  $j$  to state  $i$ , which are collected in the kinetic exchange matrix  $\mathbf{k}$ . In equilibrium

$$\frac{dM_i(t)}{dt} = 0, \quad (2)$$

and the number of all particles arriving at site  $i$  from sites  $j$  is equal to the number of all particles leaving from site  $i$  to sites  $j$  so that the total mass is conserved.

As a result of mass balance, two-site exchange between states or sites A and B always leads to symmetric 2D NMR exchange maps in thermodynamic equilibrium as the number  $k_{BA}M_A$  of particles populating site B by leaving site A per unit time is equal to the number of particles  $k_{AB}M_B$  leaving site B and populating site A per unit of time. This number is the product of the rate  $k_{BA}$  for transitions from site A to site B

60 times the population  $M_A$  of site A. The relationship  $k_{BA}M_A = k_{AB}M_B$  is known as the  
 61 ‘principle of detailed balance’. In thermal equilibrium it is understood to also apply to  
 62 rate processes involving more than two sites (Onsager 1931, Gnesotto et. al. 2018).

63 By example of mass-balanced equilibrium diffusion between three sites  
 64 (Onsager 1931, Sandstrom, 1983), Eqn. (1) becomes

$$\begin{aligned} 65 \quad k_{21}M_1 + k_{31}M_1 &= k_{12}M_2 + k_{13}M_3, \\ 66 \quad k_{12}M_2 + k_{32}M_2 &= k_{21}M_1 + k_{23}M_3, \\ 67 \quad k_{13}M_3 + k_{23}M_3 &= k_{31}M_1 + k_{32}M_2, \end{aligned} \quad (3)$$

68 or equivalently, mass balance requires

$$69 \quad k_{31}M_1 - k_{13}M_3 = k_{12}M_2 - k_{21}M_1 = k_{23}M_3 - k_{32}M_2. \quad (4)$$

70 Normalization of this expression to the total number of exchanges per unit time defines  
 71 the asymmetry parameter  $a_{sy}$  used below,

$$72 \quad (k_{23}M_3 - k_{32}M_2)/[(1,1,1) \mathbf{k} \mathbf{M}] \stackrel{\text{def}}{=} a_{sy}. \quad (5)$$

73 Here  $k_{ij}M_j$  is the number of transitions from pool  $j$  to pool  $i$ , corresponding to the peak  
 74 integral in an exchange map after correction for relaxation effects, so that the  
 75 denominator corresponds to the integral over all peaks. The asymmetry parameter  
 76 thus quantifies the imbalance of exchange between two sites in terms of the number  
 77 of unbalanced exchanges normalized to the total number of exchanges. Therefore, it  
 78 specifies the relative flux in the circular exchange process. While mass balance (4) is  
 79 a necessary condition for dynamic equilibrium, detailed balance, on the other hand, is  
 80 a stronger condition applicable to thermodynamic equilibrium. It requires

$$81 \quad a_{sy} = 0. \quad (6)$$

82 Detailed balance had been introduced by Maxwell in 1867 based on ‘sufficient  
 83 reason’ in his derivation of the speed distribution of gas atoms considering the speed  
 84 exchange between colliding gas atoms in thermodynamic equilibrium (Maxwell, 1867).  
 85 An intriguing consequence of the exchange being balanced in detail between particles  
 86 A and B amounts to the impossibility of assigning positive time to either velocity  
 87 exchange from A to B or B to A on the particle scale of the exchange process, thus  
 88 admitting negative time or time reversal. In 1872 Boltzmann showed in an elaborate  
 89 treatment, that Maxwell’s speed distribution also applies to polyatomic gas molecules  
 90 (Boltzmann, 1872). Furthermore, in 1917 Einstein derived Planck’s law of black-body  
 91 radiation as a balanced energy exchange between quantized radiation and matter  
 92 underlining the striking similarity to Maxwell’s speed distribution of gas atoms (Einstein,  
 93 1917). He concludes “Indem Energie und Impuls aufs engste miteinander verknüpft

94 sind, kann deshalb eine Theorie erst dann als berechtigt angesehen werden, wenn  
95 gezeigt ist, daß die nach ihr von der Strahlung auf die Materie übertragenen Impulse  
96 zu solchen Bewegungen führen, wie sie die Wärmetheorie verlangt," (Since energy  
97 and momentum are intimately connected, a theory can only then be considered  
98 justified, when it has been shown, that according to it the momenta of the radiation  
99 transferred to the matter lead to such motions as demanded by the theory of heat.)

100 In his work extending Maxwell's speed distribution to polyatomic gas molecules  
101 Boltzmann considered molecules in a container whereby the walls reflect the  
102 molecules like elastic balls: "Bezüglich der Gefäßwände, welche das Gas  
103 umschließen, will ich jedoch voraussetzen, dass die Moleküle an denselben wie  
104 elastische Kugeln reflektiert werden. ... Die Wände stören nicht, da an ihnen die  
105 Moleküle wie elastische Kugeln reflektiert werden; also geradeso von ihnen  
106 zurücktreten, als ob der Raum jenseits der Wände von gleich beschaffenem Gase  
107 erfüllt wäre." (Concerning the container walls which enclose the gas, I want to presume  
108 that the molecules are reflected from them like elastic balls. .... The walls do not  
109 interfere, because the molecules are reflected from them like elastic balls; that is,  
110 recede from them just like that, as if the space beyond the walls would be filled with  
111 similarly conditioned gas.) Moreover, the interaction between gas molecules can be of  
112 any type. While Boltzmann states that any other interaction between walls and  
113 molecules leads to the same result albeit at loss of simplicity, the perfectly elastic  
114 reflections of the gas molecules at the walls eliminate the topological constraints of the  
115 box on their motion. For confined particles, this means that the pressure across the  
116 pore volume is constant, i. e. the time average of the particle density does not vary  
117 with the location inside the pore. Boltzmann obtained the same speed distribution for  
118 polyatomic molecules with internal degrees of freedom as Maxwell had for atoms  
119 based on detailed balance of speed exchange. In the simulations reported below, the  
120 motion of molecules is considered for which the interactions with the walls are the  
121 same as those among the molecules. Understanding confined diffusion (Valiullin,  
122 2017) is important from a general point of view because the motion of molecules  
123 without topological constraints is an ideal limit which cannot perfectly be realized in  
124 practice although it may be realized within experimental uncertainty.

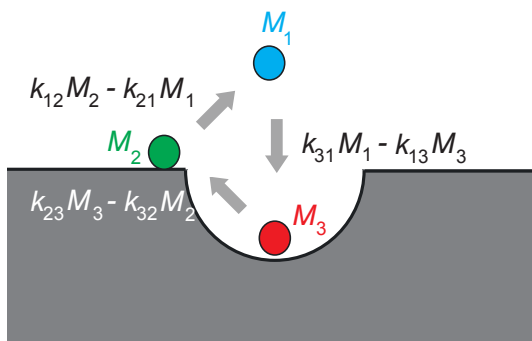
125 Two-site exchange processes will always be symmetric in equilibrium. This  
126 situation has been evaluated analytically for NMR relaxation exchange of fluids in  
127 porous media (McDonald, 2005). Yet multi-site relaxation-exchange NMR maps (Van

128 Landeghem, 2010) can formally be asymmetric in equilibrium. For example, the  
 129 transverse magnetization  $s(t_1, t_2)$  from a three-site  $T_2$ - $T_2$  relaxation exchange NMR  
 130 experiment (Gao and Blümich, 2020),

$$131 \quad s(t_1, t_2) = (1,1,1)e^{-(\mathbf{R}_2+\mathbf{k})t_2}e^{-(\mathbf{R}_1+\mathbf{k})t_m}e^{-(\mathbf{R}_2+\mathbf{k})t_1}\mathbf{M}(t_0), \quad (7)$$

132 has been simulated to model an experimentally observed asymmetric three-site  $T_2$ - $T_2$   
 133 NMR exchange map of water molecules saturating  $\text{Al}_2\text{O}_3$  powder with the three  
 134 relaxation sites corresponding to bulk water, water molecules on the surface of the  
 135 powder particles and water molecules inside the surface pores (Fig. 1). Here  $\mathbf{M}(t_0)$  is  
 136 the initial vector of transverse magnetization components from relaxation sites 1, 2 and  
 137 3 generated from longitudinal thermodynamic equilibrium magnetization with a 90°  
 138 pulse at the beginning of the experiment at time  $t_0$ , and  $t_1$ ,  $t_m$ ,  $t_2$  are the evolution,  
 139 mixing, and detection time intervals of the 2D NMR experiment, respectively  
 140 (Callaghan, 2011; Lee et al., 1993). Apart from the relaxation-rate matrices  $\mathbf{R}_1$  and  $\mathbf{R}_2$ ,  
 141 and the kinetic matrix  $\mathbf{k}$ , the best match obtained by forward simulation returned the  
 142 peak integrals revealing an asymmetry parameter of  $a_{sy} = -1.2\%$ . This asymmetry of  
 143 the forward and backward particle jumps between two sites specifies the relative  
 144 circular flux between the three sites (Fig. 1).

145



146

147 Figure 1. Asymmetry in three-site diffusion-mediated exchange indicates coherent  
 148 circular motion in a model example of water molecules in contact with a porous surface.  
 149 Three water populations  $M_j$  are identified by different NMR relaxation times and color.  
 150 They are molecules in the bulk (1), molecules on the surface (2) and molecules in the  
 151 pores (3). The exchange rate constants are  $k_{ij}$ . The net particle flux  $k_{ij}M_j - k_{ji}M_i$   
 152 between two sites differs from zero. The net mass of all molecules participating in the  
 153 exchange is conserved. The figure illustrates positive  $a_{sy}$ .

154

155 The asymmetry observed in the experiment can be argued to result from the  
 156 uncertainty of the measurement and the data processing by 2D inverse Laplace  
 157 transformation (Song 2002). Also, asymmetric three-site exchange disagrees with

158 detailed balance of the exchange between any pair of sites in thermodynamic  
159 equilibrium because it needs to be explained by circular diffusion on the pore scale,  
160 and such motion resembles that of a ratchet which Feynman has argued to disagree  
161 with the second law of thermodynamics (Feynman et al., 1966). Nevertheless, Monte  
162 Carlo simulations were executed and are discussed below to investigate asymmetry in  
163 three-site exchange.

164

## 165 **2. Modelling confined diffusion**

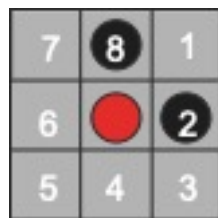
### 166 **2.1 Vacancy diffusion: Random particle jumps on a 2D checkerboard**

167 Random jumps of particles from occupied sites to vacant sites were simulated with a  
168 Monte-Carlo algorithm (Metropolis et al., 1953; Grebenkov, 2011; Hughes, 1995;  
169 Sabelfeld, 1991) in a confined space on a checkerboard. The algorithm models  
170 vacancy diffusion (Seitz, 1948) encountered in metals and alloys but the particles  
171 perform the jumps rather than the vacancies. To keep the simulation simple, it is limited  
172 to jumps on a 2D  $3\times 3$  Moore lattice of range 1 (Wolf-Gladrow, 2000) following rules of  
173 the game of life (Wolf-Gladrow, 2000; Bialnicki-Birula, 2004). Here the center particle  
174 can jump to any of its 8 neighbors (Fig. 2). Different neighborhoods of range 1 were  
175 tested (Fig. S1) (Bialnicki-Birula, 2004), but only the Moore neighborhood having the  
176 highest symmetry of all neighborhoods, produced data consistent with Eqn. (4).  
177 Topological constraints are introduced which set boundaries to the jump space.  
178 Initially, the available cells inside the jump space on the grid are populated randomly  
179 with particles up to a specified particle density. Particles in the bulk are indexed 1, and  
180 two distinct boundary sections are indexed 2 and 3, giving three environments for the  
181 particles to be exposed to and between which randomly selected particles can move.  
182 A particle jumping from environment  $j$  to  $i$  is counted by incrementing the element  $ij$  of  
183 a  $3\times 3$  jump matrix with elements  $k_{ij}M_j$  by 1. If the particle environment does not  
184 change with the jump, the respective diagonal element  $k_{jj}M_j$  is incremented. The NMR  
185 relaxation environments are indexed according to increasing relaxation rate. If a  
186 particle is in contact with two different relaxation environments, it is assigned to the  
187 relaxation environment with the higher index according to the higher relaxation rate.

188 Different rules governing jumps to a neighbor cell were explored. 1) In the  
189 simplest case, one of the 8 destination cells was chosen at random without assigning  
190 a jump probability. When destination cell was free, the jump was executed, and the  
191 initial and final environments were compared to increment the corresponding entry in

192 the jump matrix accordingly. When the destination cell was occupied, the particle  
193 remained at its source cell, and the respective diagonal element of the jump matrix  
194 was incremented. In all other cases, jump probabilities were assigned. 2) As a subtle  
195 variant of the random jumps to any of the 8 neighbor cells, jumps were randomly  
196 selected to any of the *free* neighbor cells by assigning zero jump probability to occupied  
197 neighbor cells and equal probability for jumps to the empty cells. This algorithm is  
198 known to violate detailed balance (Metropolis et al., 1953; Reviewer, 2023). 3) With  
199 reference to the Helmholtz free energy  $A = U - TS$ , where  $U$  is internal energy,  $T$  is  
200 temperature, and  $S$  is entropy, a jump probability  $p = \exp\left\{-\frac{\Delta A}{k_B T}\right\}$  was introduced,  
201 where  $\Delta A = \Delta U - T \Delta S$ ,  $T$  is the temperature, and  $k_B$  the Boltzmann constant.  $\Delta U =$   
202  $-\mathbf{F} \Delta \mathbf{R}$  and  $\Delta S$  were estimated from the sum of distances to free or occupied neighbor  
203 cells by crude empirical models as detailed in the supporting information. Here  $\mathbf{F}$  is the  
204 force and  $\Delta \mathbf{R}$  the distance vector between two particles. This allowed probing attractive  
205 and repulsive interactions by changing the sign of  $\Delta U$  in simulation runs and varying  
206 temperature in addition to varying population density equivalent to pressure. It is noted  
207 here that the force field on a randomly populated lattice is not conservative (Reviewer,  
208 2023). In other words, the energy balance of a particle moving in a circle is different  
209 from zero, and Monte Carlo simulations under these constraints probe a driven  
210 equilibrium and not thermodynamic equilibrium (Michel et. al., 2014).

211



212

213 Figure 2. Jumps on a checkerboard grid modelling vacancy diffusion. The center  
214 particle can jump to any of its eight next nearest neighbor cells, which are numbered  
215 clockwise from 1 to 8. Jump probabilities were introduced to account for particle  
216 interaction between the center particle (red) and neighbor particles (black).

217

218 The vacancy-diffusion simulations were carried out with a program written in  
219 Matlab R2020a by The MathWorks Inc. on an Apple MacBook Pro 2.4 GHz having an  
220 Intel Quad-Core i5 processor. Unless indicated otherwise,  $10^7$  jumps were simulated  
221 in one run taking 75 seconds.

222

223 **2.2 Gas diffusion**

224 The gas diffusion calculations explore similar pore size and occupancy. Here the  
 225 motion of circular particles with diameter equal to the cell size was accomplished by  
 226 propagating an initial distribution of particle speeds for random initial positions and  
 227 directions in a Monte Carlo fashion based on instantaneous collisional forces. This  
 228 distribution rapidly equilibrated to a Maxwell-Boltzmann distribution. Whereas in  
 229 vacancy-diffusion simulations the distribution of particles in the pore is recorded after  
 230 each jump it is recorded in the gas-phase simulations at constant time intervals. If the  
 231 center of each particle was within one diameter of another, the particles are considered  
 232 to have collided. Immediately after a collision the projection of the velocity vector along  
 233 the collision axis is reversed prior to propagating to the next step. In this approach, the  
 234 observation time interval must be sufficiently small, so that the new velocities are  
 235 calculated with a small position uncertainty of the colliding particles (Reviewer 2023,  
 236 Michel et al. 2014).

237 The collisions change both the direction and velocity of the particles at each of  
 238 the  $10^9$  constant time increments used here. Following conservation of momentum and  
 239 kinetic energy,

$$240 \quad \vec{v}_{1,\text{new}} = \vec{v}_{1,\text{old}} - \frac{2m_2}{(m_1+m_2)} \frac{\langle \vec{v}_{1,\text{old}} - \vec{v}_{2,\text{old}}, \vec{x}_1 - \vec{x}_2 \rangle}{\|\vec{x}_2 - \vec{x}_1\|^2} (\vec{x}_1 - \vec{x}_2), \quad (8)$$

$$241 \quad \vec{v}_{2,\text{new}} = \vec{v}_{2,\text{old}} - \frac{2m_1}{(m_1+m_2)} \frac{\langle \vec{v}_{2,\text{old}} - \vec{v}_{1,\text{old}}, \vec{x}_2 - \vec{x}_1 \rangle}{\|\vec{x}_2 - \vec{x}_1\|^2} (\vec{x}_2 - \vec{x}_1). \quad (9)$$

242 These collisions with other particles and the wall are mediated by the particle size,  
 243 which is set to be a fraction of the pore-side length of one. This means that a square  
 244 pore with a five-particle diameter side length is populated with particles having a  
 245 diameter of 1/5. To compare the continuous positional output of this model to vacancy  
 246 diffusion, a two-dimensional square grid with cell size set by the particle diameter is  
 247 imposed on the entire pore. The quasi-continuous positional output is then binned into  
 248 these cells and compared to the binned positions from the previous observation to  
 249 determine if particles translated between the main pore volume, pore wall, and active  
 250 site. The translational information is used to assign estimates of the jump-matrix  
 251 elements and thus the asymmetry parameter  $a_{sy}$ .

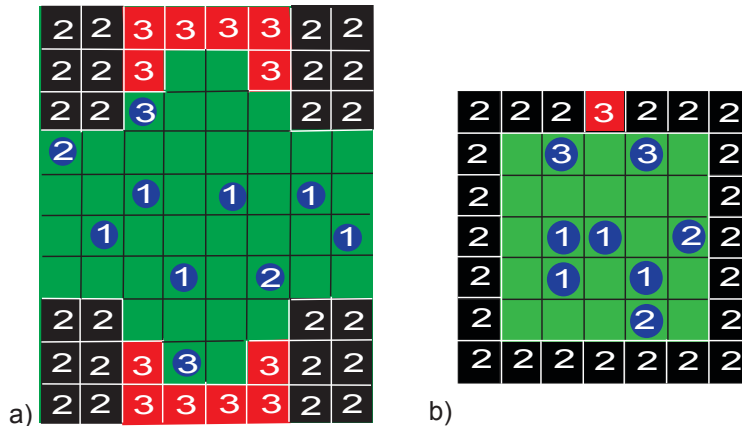
252 The gas-diffusion simulations were carried out with a program written in Matlab  
 253 R2020a by The MathWorks Inc. on a home-built desktop computer possessing an  
 254 AMD Ryzen 7 2700 processor. In most cases,  $10^9$  jumps were simulated in one  
 255 run taking roughly 45 hours to complete.

256

257 **3. Results**

258 Two different pore geometries were analyzed. Initially, the simulation was executed for  
 259 a pore geometry (Fig. 3a) which approximates the surface structure of Fig. 1, and  
 260 which is hypothesized to explain the observed asymmetry of water diffusing in a porous  
 261  $\text{Al}_2\text{O}_3$  grain pack (Gao and Blümich, 2020). The dented surface was mirrored  
 262 horizontally to double the probability of particles entering the dent (relaxation site 3) in  
 263 the otherwise straight surface (relaxation site 2). The bulk of the particles defines  
 264 relaxation site 1. Periodic boundary conditions were employed right and left. A pore  
 265 boundary has been treated just like an occupied cell with the same rules applying to  
 266 the jump probability. The simulations of particle motion confined to this complex pore  
 267 structure and constrained by jump probabilities revealed the existence of asymmetric  
 268 exchange. To understand the essence of the asymmetry the pore geometry was  
 269 simplified to a square with an active site in the wall to study particle motion in detail.  
 270 Particles in the bulk, in contact with the walls, and with the active site are identified by  
 271 different NMR relaxation properties (Fig. 3b).

272



273

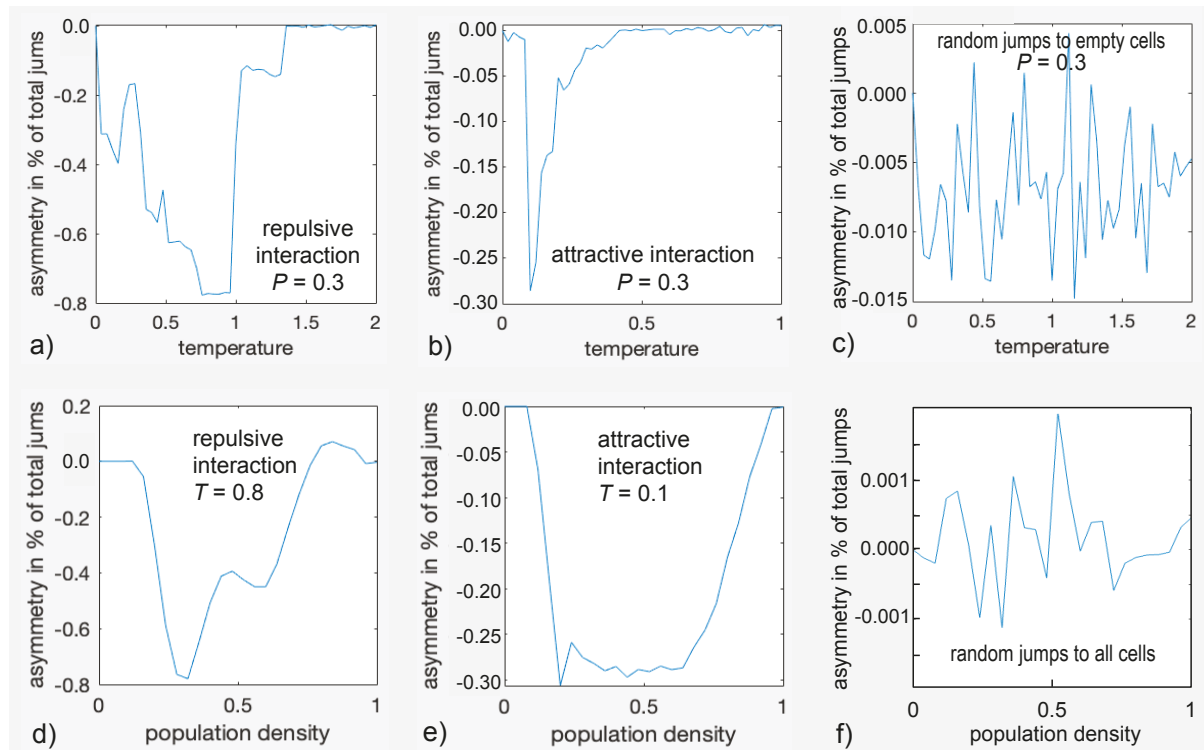
274 Figure 3. Examples of pore models for two-dimensional three-site exchange based on  
 275 a checkerboard grid. Particles can occupy one cell and jump to a neighboring one  
 276 following different realizations of the jump probability. a) Porous solid. The boundaries  
 277 right and left are periodic. The boundaries top and bottom are rigid. Depending on their  
 278 next neighbors in the first coordination shell, the particle-relaxation environments are  
 279 identified as bulk (1), surface (2), and pore (3) with increasing relaxation rate. b) Small  
 280 square pore with an active site. The bulk (1), the walls (2), and the active site (3) have  
 281 different relaxation properties. If a particle is in contact with two different relaxation  
 282 sites, it is counted to belong to the particle pool with the larger relaxation rate, i. e. the  
 283 pool with the higher number.

284

285 Enabled by the interaction model, which, depending on the particle environment  
 286 assigns different jump probabilities as a function of temperature, the asymmetry

287 parameter  $a_{sy}$  was evaluated for both pores with the vacancy-diffusion algorithm as a  
 288 function of temperature  $T$  and pressure  $P$ . Pressure was varied in terms of the  
 289 population density measured as the fraction of cells occupied in the pore. The results  
 290 for the complex pore are reported in the supplementary material (Fig. S3), whereas  
 291 those for the simple square pore are reported in the main text here (Fig. 4). At certain  
 292 temperatures and pressures also the autocorrelation function of the occupation-time  
 293 track of a particular cell and its Fourier transform were determined. Striking features  
 294 observed in vacancy diffusion were subsequently modelled with the gas-diffusion  
 295 algorithm in the square pore.

296



297

298 Figure 4. Asymmetry parameters  $a_{sy}$  for diffusion inside the small rectangular pore  
 299 depicted in Fig. 3b as a function of temperature  $T$  (a-c) and pressure  $P$  (d-f). a)  $a_{sy}(T)$   
 300 for repulsive interaction at  $P = 0.3$ . b)  $a_{sy}(T)$  for attractive interaction at  $P = 0.3$ .  
 301 c)  $a_{sy}(T)$  for jumps to randomly selected empty cells. d)  $a_{sy}(P)$  for attractive interaction  
 302 at  $T = 0.8$ . e)  $a_{sy}(P)$  for attractive interaction at  $T = 0.1$ . f)  $a_{sy}(P)$  for jumps to cells  
 303 randomly selected from all eight neighbor cells.

304

305 Relevant results for the square pore (Fig. 3b) are summarized in six graphs in  
 306 Fig. 4. The asymmetry parameter varies strongly with temperature  $T$  (Figs. 4a,b) and  
 307 pressure corresponding to population density  $P$  (Figs. 4d,e). All parameters are relative  
 308 quantities without units. The top three graphs a), b) and c) show the variation of  $a_{sy}$   
 309 with temperature for a population fraction of 0.3 corresponding that of a gas. The

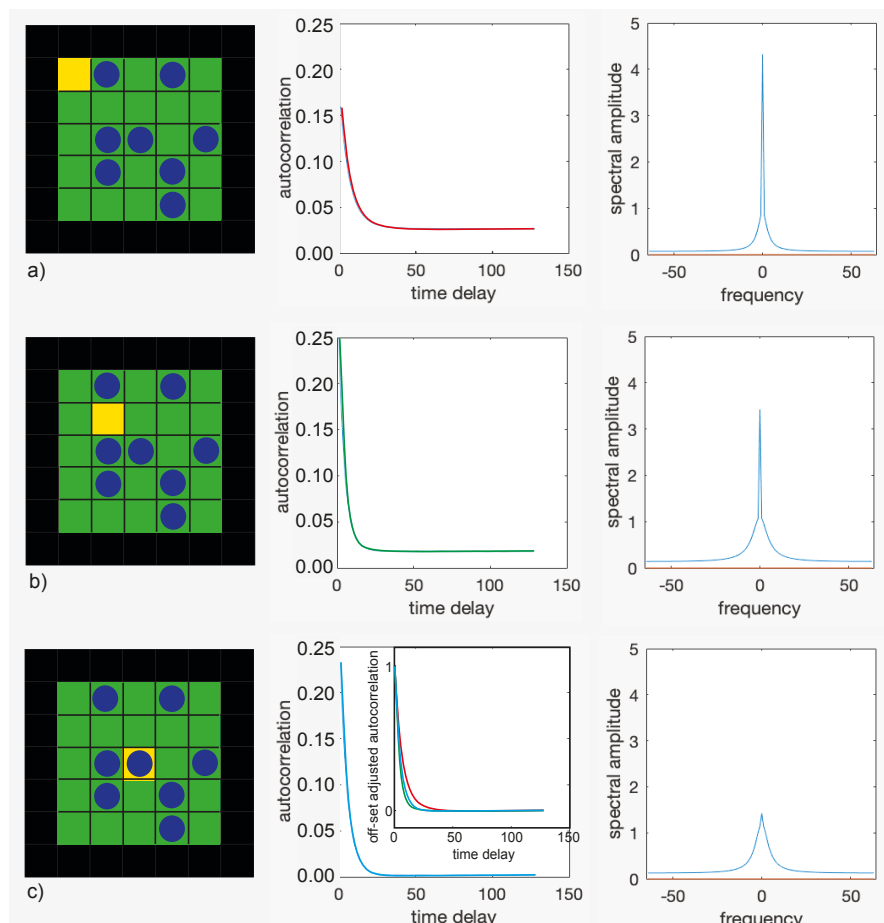
310 asymmetry parameter assumes only negative values in an abrupt but reproducible  
311 manner in the range of  $-0.8\% < a_{sy} < 0.0\%$  for repulsive interaction (Fig. 4a), i. e. for  
312 the definition of the force between particles as illustrated in Fig. S2a. With reference to  
313 Fig. 1, negative  $a_{sy}$  reports that the straight exit route from the active site towards the  
314 center of the pore is preferred over the detour via the pore wall. When the interaction  
315 is changed from repulsive to attractive by inverting the sign of  $\Delta U$  in the expression for  
316 the free energy, the asymmetry parameter varies as well, however, only between  $-$   
317  $0.3\% < a_{sy} < 0.0\%$  (Fig. 4b). In either case, the asymmetry parameter varies with  
318 temperature and pressure. It is concluded, that for this small pore, up to about 1% of  
319 all jumps on the checkerboard can proceed in an ordered circular fashion between the  
320 three sites. Similar behavior is observed for the complex pore of Fig. 3a as illustrated  
321 in Fig. S3 in the supplement.

322 At the extrema of the  $a_{sy}(T)$  curves in Figs. 4a,b the dependence of the  
323 asymmetry parameters on population density was investigated (Figs. 4d,e). The  
324 variations with population density are smoother than those with temperature.  
325 Significant negative asymmetry results at intermediate pressure, while at low and high  
326 pressure, the asymmetry is small (Fig. 4d,e). At higher temperature and high pressure,  
327 small positive  $a_{sy}$  is observed (Fig. 4d,  $T = 0.8$ ,  $P = 0.8$ ). If the destination cell for a  
328 jump is chosen at random without considering a hypothetical free jump energy  $A$ ,  
329 essentially noise more than two orders of magnitude smaller is observed for the  
330 exchange asymmetry determined from  $10^7$  jumps when varying  $T$  and  $P$  (Fig. 4c,f).  
331 However, a small bias towards negative  $a_{sy}$  results if the destination cell is chosen at  
332 random from all free neighbor cells (Figs. 4c), whereas no bias is detected if the  
333 destination cell is chosen at random from all neighbor cells whether free or occupied  
334 (Fig. 4f). This difference becomes more pronounced at higher number of jumps (see  
335 below).

336 To shed further light on the origin of the asymmetry, autocorrelation functions of  
337 the occupation-time tracks of selected cells in the pore were computed and Fourier  
338 transformed (Fig. 5). The occupation-time track was calibrated to zero mean for purely  
339 random occupation, i. e. it contained the negative population density when it was empty  
340 and the complement of the population density to one when the cell was occupied. The  
341 faster the autocorrelation function decays, the less coherent the cell population  
342 fluctuates and the broader is its Fourier transform, i. e. the transfer function (Fig. 5b,c).  
343 A constant offset of the autocorrelation function shows that the time-average

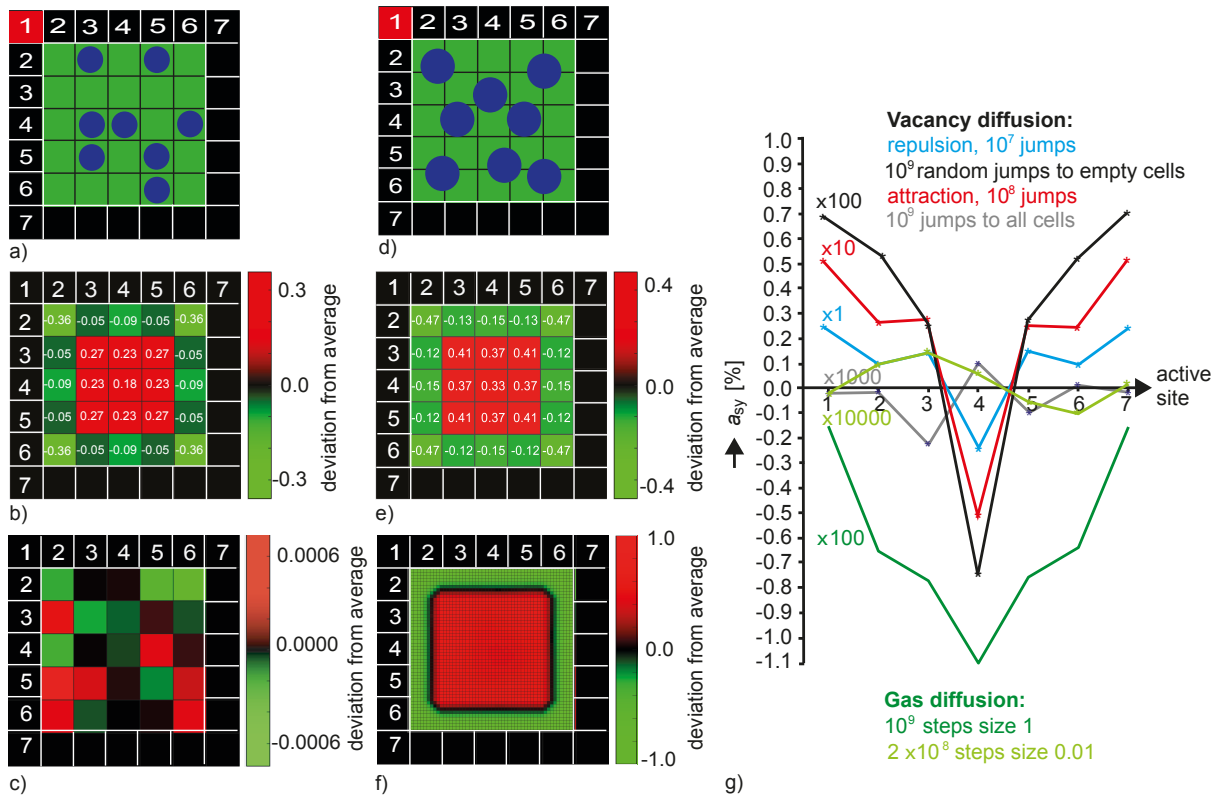
344 population in the cell differs from the mean population of the pore (Fig. 5a,b). This  
 345 offset produces a spike at zero frequency in the transfer functions. Subtracting the  
 346 offsets from the autocorrelation functions and scaling the resulting functions to the  
 347 same amplitude reveals different decays in different cells and thus variations in particle  
 348 dynamics across the pore (inset in Fig. 5c, middle). These dynamics cannot readily be  
 349 measured for a single cell in the pore, although an average over all cells and pores in  
 350 the measurement volume would be amenable to experiment by probing the particle  
 351 dynamics with CPMG measurements in magnetic gradient fields at variable echo time.  
 352 Such measurements provide the frequency-dependent diffusion coefficient in terms of  
 353 the Fourier transform of the velocity autocorrelation function (Stepišnik et al., 2014,  
 354 Callaghan and Stepišnik, 1995; Parsons et al., 2006).

355



356

357 Figure 5. Autocorrelation functions (center) of the occupancy of the yellow cells (left)  
 358 and the real parts of their Fourier transforms (right) for repulsive interaction at  $T = 0.1$   
 359 and  $P = 0.3$ . a) Corner cell. b) Off-center cell. c) Center cell. The inset in the middle  
 360 compares the decays of all three autocorrelation functions after subtraction of the  
 361 offsets.  
 362



363

Figure 6. Population density distributions and dependences of the asymmetry parameter  $a_{sy}$  on the position of the active relaxation site in the wall of a pore with  $5 \times 5$  cells. a) Vacancy diffusion. Particles can jump one step on the grid in 8 directions. b) Deviations from average relative density 1 for  $10^9$  jumps chosen at random to any of the free neighbor cells. c) Deviations from average relative density 1 for  $10^9$  jumps chosen at random to any of the 8 neighbor cells. d) Gas diffusion. The particle motion is computed on a fine grid. e) Deviations from average relative density 1 for  $10^9$  observations of particle positions at observation intervals of duration 1. The particle position at the time of observation is binned to the coarse vacancy-diffusion grid. f) Deviations from average relative density 1 on a fine  $50 \times 50$  grid of 0.1 particle diameters for  $10^9$  observations of particle positions at observation intervals of duration 0.01. g) Variations of the asymmetry parameter with the position of the active site in the cell wall for differently interacting particles for vacancy diffusion at  $T = 0.2$ ,  $P = 0.3$ , and different jump probabilities as well as for gas diffusion at long and short observation intervals of 1 vs. 0.01. The mirror symmetry of each trace about the center position reports high precision of the simulation.

380

While the autocorrelation function is difficult to probe experimentally, the asymmetry parameter  $a_{sy}$ , on the other hand, probes the particle dynamics and could be investigated experimentally directly by relaxation-exchange NMR experiments provided the signal-to-noise ratio is good enough. The parameter depends on the location of the relaxation center in the pore wall (Fig. 6). This dependence has been verified to be identical for all walls of the square pore. Moreover, it exhibits mirror symmetry about the center position (Fig. 6g), assuring that the simulation noise is negligible. For vacancy diffusion in a  $5 \times 5$  square pore with walls 7 cells wide (Fig.

6a,b),  $a_{sy}$  varies consistently with position when the jumps are selected following a *priori* defined probabilities, irrespective of the particle interaction being positive, negative, or the destination cell having been chosen randomly from all free neighbor cells. But the magnitude of  $a_{sy}$  depends strongly on the selection rule defined by the jump probability as indicated in Fig. 6g by the scaling factors. It is highest at the corner positions and lowest at the center position. For random jumps to empty cells,  $a_{sy}$  is more than an order of magnitude smaller than for repulsive interaction, so that the number of particle jumps had to be increased to  $10^9$  resulting in 3 h computation time for each data point in the corresponding trace (black) Fig. 6e. Interestingly, for gas diffusion (Fig. 6d)  $a_{sy}$  varies at long observation interval (green, Fig. 6g) in a fashion similar to that for vacancy diffusion, is of magnitude comparable to that of vacancy diffusion (black, Fig. 6g), but does not change sign with position of the active site in the pore wall. In all these cases the precision of the asymmetry parameter  $a_{sy}$  obtained in the simulations exceeds the second relevant digit. If the jumps in the vacancy diffusion simulations are chosen without bias from a jump probability no exchange asymmetry is detected, only noise nearly more than one order of magnitude lower than for jumps selected at random to one of the free neighbor positions (grey, Fig. 6g). Similarly, the asymmetry parameter decreases with the observation time becoming shorter by more than two orders of magnitude as illustrated in Fig. 6g for a long time step of 1 (dark green) versus a short time step of 0.01 (light green) in simulation units of  $(m s^2 / k_B T)^{1/2}$ .

The particle dynamics manifested in  $a_{sy}$  are accompanied by variations of the average population density across the pore which is depleted in the contact layer of the particle with the pore wall, enhanced in the next layer, and tapers off towards the pore center in both cases (Figs. 6b,e, Fig. S4). The densities vary in a similar fashion across the pore for both types of diffusion albeit having somewhat different values as can be verified by close inspection of the numbers in each cell in Figs. 6b,e. These density variations disagree with Boltzmann's argument, that elastic collisions with the walls effectively remove the impact of the walls to the effect, that the walls can be neglected. Agreement, however, is reached, if the destination cells for particle jumps in vacancy diffusion are chosen at random from all and not just the free neighbor cells (Fig. 6c; Metropolis et al., 1953). Shortening the observation interval in the gas-diffusion simulations, however, maintains the unphysical density distribution across the pore and has no effect due to binning the particle positions to the vacancy-diffusion

423 grid at the time of observation, as the exact moment of a particle collision cannot be  
424 determined on a discrete time axis. On a finer grid, however, the population density is  
425 homogeneous except for the regions close to the walls, which the center of the circular  
426 particles cannot approach (Fig. 6f). If, however, projected onto the coarse vacancy-  
427 diffusion grid the population-density modulations (Fig. 6e) reappear, because the exact  
428 locations of collisions cannot be determined in a simple way at finite observation-time  
429 intervals. Nevertheless, for both algorithms, the asymmetry parameter approaches  
430 zero for all positions along the wall of the square pore (Fig. 6g, light green), confirming  
431 that detailed balance is observed.

432 The maps in Fig. 6b,c,e,f revealing the deviation of local population density from  
433 average population density were calculated by summing the 2D maps of particle  
434 locations after each jump or at each observation time, normalizing the resultant maps  
435 to the number of jumps and the particle density and subtracting the average mean  
436 expected for a constant particle density across all cells in the pore. Further maps of  
437 population density variations for the two different pores of Fig. 3 with other sizes and  
438 interaction parameters are summarized in Fig. S4 of the supplement. While the particle  
439 density varies less with temperature for vacancy diffusion, different density patterns  
440 are found at different pressures. The strongest density variations are near the pore  
441 wall whether the interaction is repulsive, attractive, or based on prior knowledge that a  
442 neighbor cell is occupied. This becomes particularly evident for larger pores (Figs.  
443 S4b,d,e). Coincidentally, at low density the main features of the density maps are  
444 strikingly similar for vacancy diffusion with destination cells chosen randomly from  
445 among the free neighbor cells (Figs. S4b) and gas diffusion (Figs. S4d). The particle  
446 density is strongly depleted at the pore corners and near the wall and significantly  
447 increased in the next particle layer (Figs. S4e,f). For interacting particles, this  
448 concentration variation is carried forward in vacancy diffusion with increasing distance  
449 from the wall leading to concentration waves which taper off towards the center of the  
450 pore and interfere with each other coming from different directions. For small pores  
451 interference patterns dominate the density distribution across the pore (Figs. 6b,e and  
452 Figs. S4a,c). For particles jumping randomly to empty neighbor cells, the decay of the  
453 concentration wave towards the pore center is fast with few to no oscillations towards  
454 the pore center, while the oscillations are enhanced by conditioning the jump  
455 probability with a hypothetical free jump energy (Fig. S4d,  $P = 0.2$ ). In particular, the

456 population density at the active site in the dent of the complex pore of Fig. 3a depends  
457 on the parameters  $P$  and  $T$  (Figs. S4a,b).

458

#### 459 **4. Discussion**

460 Confined two-dimensional diffusion has been modelled by two different algorithms to  
461 investigate in how far the cross-peaks in 2D  $T_2$ - $T_2$  exchange maps can be asymmetric.  
462 The asymmetry is quantified by an asymmetry parameter  $a_{sy}$  which reports the relative  
463 flux between two sites corresponding to the difference in the number of forward and  
464 backward exchanges normalized to the total number of exchanges. The vacancy-  
465 diffusion algorithm models particle jumps on a checkerboard grid to nearest neighbor  
466 cells under the constraint of different jump probabilities and samples the population  
467 map after each jump. The jump probability was determined from a Boltzmann  
468 distribution with a heuristic free energy which depends on the populations of the  
469 surrounding cells. The asymmetry parameters turned out to be equal to zero in the  
470 case of equal jump probability to all neighbor cells (Metropolis et al., 1953), whether  
471 occupied or not, confirming the validity of detailed balance (Fig. 6g). It was found to be  
472 different from zero when different jump probabilities were assigned to different  
473 neighbor cells, i. e. when the jump energy depended on the population pattern of the  
474 neighbor cells. But with the statistical arrangement of the particles on a checkerboard  
475 and the confinement of the interaction force to next nearest neighbors, energy is not  
476 conserved with a particle move, so that each particle move either injects or extracts  
477 energy from the system. Nevertheless, the equilibrium condition (3) is fulfilled, so that  
478 the system is not in thermodynamical equilibrium but rather in an equilibrium that is  
479 driven by the algorithm. The observed asymmetry parameter is, therefore, assigned to  
480 a driven and not thermodynamic equilibrium.

481 The gas-diffusion algorithm models particles colliding with initial velocity vectors  
482 and calculates new velocity vectors after a collision from conservation of energy and  
483 momentum, whereby the instant of a collision is interrogated on a discrete time grid.  
484 The smaller the observation time, the more precise the instant of a collision is  
485 determined. Any deviation from the exact collision time leads to errors in the position  
486 coordinates of the colliding particles and thus their velocities (Eqns. 7,8; Michel et al.  
487 2014). While for large observation time a significant asymmetry parameter is observed  
488 (Fig. 6g, dark green) its value shrinks drastically when the observation time is reduced  
489 by a factor of 100 (Fig. 6g, light green). It is concluded that in the limit of infinitely short

490 observation time, also the gas-diffusion algorithm can produce vanishing asymmetry  
491 parameter in three-site exchange in agreement with the principle of detailed balance  
492 and with symmetry in the cross-peak intensities of exchange maps in thermodynamic  
493 equilibtium. If, on the other hand, the velocities are calculated with a systematic error  
494 in the gas-diffusion model due to a finite observation interval, the resultant velocities  
495 disagree with the energy and momenta of elastic collisions, so that also here energy  
496 is injected or extracted from the system and the observed asymmetry parameter can  
497 be attributed to a driven and not a thermodynamic equilibrium.

498 The asymmetry parameters observed for either of the two pore shapes (Fig. 3)  
499 investigated with the vacancy-diffusion model vary in a range on the order of  $-1\% < a_{sy} < 1\%$ , i. e., up to 1% of all particles in the pore do not follow detailed balance  
500 between all pairs of sites but move coherently in circles between the three sites. It is  
501 emphasized that this circular exchange is between the pools of particles representing  
502 the three sites, and it is not a motion followed by individual particles completing circular  
503 jumps. Given repulsive or attractive interaction in the vacancy diffusion model with  
504 heuristic temperature and pressure dependent jump probabilities, the variations of  $a_{sy}$   
505 with temperature  $T$  appear rapid, reminiscent of phase transitions (Figs. 4a,b, Figs.  
506 S3a). The variations of  $a_{sy}$  with pressure corresponding to population density  $P$  are  
507 smooth (Figs. 4d,e, Figs. S3b). Either positive or negative values of  $a_{sy}$  are observed  
508 as  $T$  or  $P$  change. A sign change of  $a_{sy}$  reports a change in the sense of the circular  
509 exchange (cf. Fig. 1).

511 For a simple square pore, the asymmetry parameter varies with the position of  
512 the active site in the cell wall, exhibiting mirror symmetry with respect to the wall center  
513 (Fig. 6g). The variation is the same for the different jump probabilities, referred to as  
514 repulsive and attractive interaction or random jumps to empty cells albeit it differs  
515 significantly in magnitude. A similar dependence is observed in the gas-phase diffusion  
516 simulations at long observation time. Moreover, the autocorrelations functions and  
517 their Fourier transforms have been determined for the occupancy time tracks of  
518 selected cells at specific positions inside a small square pore for  $10^7$  jumps of all  
519 particles in the pore (Fig. 5). The time-track function had been devised to have zero  
520 mean for the average cell population. Depending on the position of the cell inside the  
521 pore, the autocorrelations functions and their Fourier transforms vary. Specifically, the  
522 autocorrelation function can exhibit a significant constant offset. At these positions  
523 inside the pore, the particle densities are different from the pore average, and the cell

524 is on average emptier or more occupied than expected if the exchange between all  
525 cells were the same. This conclusion is supported by the observed deviations of the  
526 cell occupancies from the pore average (Figs. 6b,e, Fig. S4). Near the pore wall the  
527 average population density is depleted and varies in an oscillatory manner along the  
528 pore wall. Further towards the center of the pore the average population density  
529 increases sharply and then tapers off towards the pore center to a value slightly above  
530 the average density.

531 These observations for driven vacancy diffusion in a square pore with  $5 \times 5$  cells  
532 are compared to independent simulations of driven gas diffusion (long observation  
533 time: step size 1) of non-interacting particles in a square pore with an edge length of 5  
534 particle diameters also allowing 7 relaxation centers along the pore wall (Figs. 6a,d).  
535 A similar variation of the asymmetry parameter is found as for vacancy diffusion, but  
536 the asymmetry parameter is negative for all positions of the active site (Fig. 6g, dark  
537 green). Moreover, the depletion of the average particle density at the pore wall and its  
538 subsequent variation towards the center are similar with the exception, that oscillations  
539 of the average particle density along the pore wall are weaker for gas diffusion for the  
540 (Figs. 6b,e). These oscillations persist even at short observation times due to the  
541 uncertainty of localizing the particle positions at the exact time of their collision on a  
542 discrete time grid. The lack of a sign change in the asymmetry parameter with changing  
543 position of the active site may be explained by destructive interference of particle  
544 collisions from multiple sites with the wall within one discrete particle diameter and the  
545 fact, that the free path length between collisions in gas diffusion is not limited to the  
546 next cell as in vacancy diffusion but can range up to the pore diameter. Taken together,  
547 the observed asymmetry in the three-site exchange in driven equilibrium and the  
548 variation of the jump statistics with position inside the pore point at diffusive resonance  
549 phenomena like standing waves of air in pipes as reported by Kundt (Kundt, 1866) or  
550 of vibrating plates as reported by Chladni (Chladni, 1787).

551 Three-site exchange can be viewed as a finite difference approximation to the  
552 Laplace operator (van Kampen, 1992; Kuprov, 2022) governing Fick's second law  
553 (Fick, 1855). Considering some local site  $N$  with neighbor sites  $N-1$  and  $N+1$  right and  
554 left, the mass flow to and from site  $N$  given by Eqn. (1) is

$$555 \quad \frac{dm_N(t)}{dt} = k_{N,N-1}m_{N-1} - k_{N-1,N}m_N + k_{N,N+1}m_{N+1} - k_{N+1,N}m_N, \quad (10)$$

556 Taking the limit to infinitesimal small distance  $\Delta r \rightarrow dr$  between the neighboring sites  
 557 leads to  $k_{j,i} = k$ , revealing that (10) is a finite difference approximation of a second  
 558 spatial derivative balanced by the temporal variations of  $m$  during infinitesimal time  $dt$ ,

$$559 \quad (k m_{N-1} - 2 k m_N + k m_{N+1})/\Delta r^2 \approx k \frac{d^2 m}{dr^2} = \frac{dm}{dt} / \Delta r^2. \quad (11)$$

560 In this limit, Eqn. (11) becomes Fick's second law with the diffusion coefficient  $D =$   
 561  $k \Delta r^2$ . This back-of-the-envelope argument suggests that the observed asymmetry of  
 562 three-site exchange is a property of Fick's second law and relates to eigenmodes of the  
 563 Laplace operator (Hoop and Prange 2007, Grebenkov and Nguyen 2013).

564 The diffusion equation applicable to longitudinal magnetization in NMR instead of  
 565 particle masses  $m$  is the Bloch-Torrey equation (Torrey, 1956),

$$566 \quad \frac{\partial}{\partial t} m(\mathbf{r}, t) = D \nabla^2 m(\mathbf{r}, t) - \mu m(\mathbf{r}, t), \quad (12)$$

567 where  $m$  now is the magnetization deviation from thermal equilibrium and  $\mu$  is the bulk  
 568 relaxation rate.  $m(\mathbf{r}, t)$  solves this equation in terms of an expansion into normalized  
 569 eigenfunctions  $\phi_n(\mathbf{r})$  with amplitudes  $A_n$  and eigenvalues  $\tau_n$  (Brownstein and Tarr,  
 570 1977; Song, 2000)

$$571 \quad m(\mathbf{r}, t) = e^{-\mu t} \sum_{n=0}^{\infty} A_n \phi_n(\mathbf{r}) e^{-\frac{t}{\tau_n}}. \quad (13)$$

572 The eigenvalues are determined by the boundary condition

$$573 \quad D \mathbf{n} \nabla \phi_n(\mathbf{r}) = \rho \phi_n(\mathbf{r}), \quad (14)$$

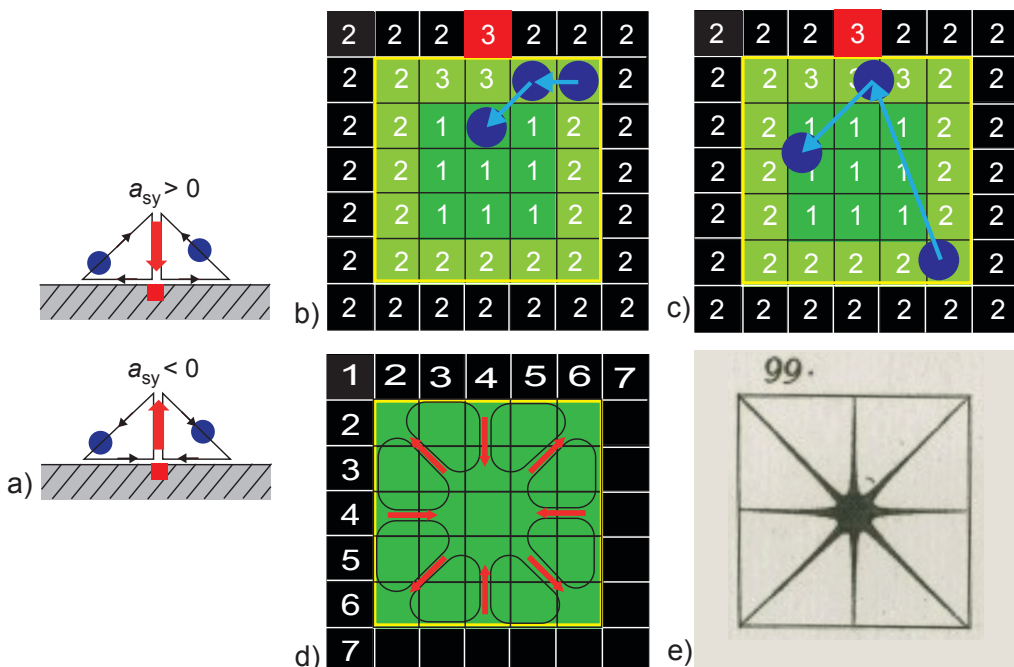
574 where  $\rho$  is the surface relaxivity and  $\mathbf{n}$  is the unit vector normal to the surface. They  
 575 depend on the diffusion coefficient and determine the NMR relaxation time in different  
 576 ways according to the pore geometry. The population  $\phi_0$  of the lowest normal mode  
 577 has no nodes. The higher normal modes  $\phi_n$  possess nodal surfaces. The higher  
 578 diffusion eigenmodes have been detected by NMR with selective excitation of partial  
 579 pore volumes making use of field gradients internal to the pore (Song, 2000). These  
 580 experimental results reported by Song agree with the Monte Carlo simulations of driven  
 581 diffusive translational motion in pores reported here, in that the population density  
 582 varies across the pore and that the offset of the autocorrelation function of the local  
 583 pore occupancy depends on the position of the cell in the pore. It needs to be  
 584 investigated further how much the NMR relaxation times and the associated particle  
 585 dynamics vary with the position from the pore wall to the center in the driven  
 586 concentration wave (Bytchenkoff and Rodts, 2011). On the other hand, stochastic  
 587 resonance in thermodynamic equilibrium has been observed with NMR first by Sleator,  
 588 Hahn et al. (Sleator et al., 1985) and subsequently studied in detail by Müller,

589 Jerschow, et al. in different scenarios (Müller and Jerschow, 2005; Schlagnitweit and  
590 Müller, 2012). There, the magnetization fluctuating with the thermal motion of the  
591 nuclear spins assumes the role of the particles and the resonance circuit assumes the  
592 role of the pore. Diffusion eigenmodes are expected to be unobservable with this  
593 method unless a subset of modes is driven by an external stimulus, because they are  
594 silent in thermodynamic equilibrium.

595 From the exchange asymmetry of the particles in the square pore investigated in  
596 Fig. 6 a suggestive picture emerges for driven confined vacancy diffusion (Fig. 7),  
597 where the diffusion lengths are confined to the distances from the particle to the direct  
598 neighbor cells. Depending on the sign of the asymmetry parameter (Fig. 7a), a small  
599 fraction of the particles (blue circles) prefers the direct path towards or away from the  
600 active site (red square) at the pore boundary over the path along the boundary to or  
601 from the active site. In the center of the wall, the direct path away from the active site  
602 to the bulk is preferred over the path along the pore wall when leaving the contact  
603 region with the active site (Fig. 7b). But because jumps are allowed in vacancy diffusion  
604 only to neighboring cells, the cells belonging to relaxation pool 2 at the wall right and  
605 left of the active site 3 must be populated from the bulk 1 by direct jumps from the bulk  
606 to the wall. For these jumps, the asymmetry parameter is indeed positive, as observed  
607 for the off-center positions of the active site (Fig. 6g). Given the symmetry of the square  
608 pore, the in-plane translational diffusion paths resulting from the variation of the  
609 asymmetry parameters with the position of the active site on the pore wall demand the  
610 existence of eight diffusion vortices inside the planar pore (Fig. 7d). The symmetry of  
611 this in-plane translational diffusion pattern matches the symmetry of one of the node  
612 patterns of the out-of-plane vibrational modes of a square plate observed by Chladni  
613 (Fig. 7e) about a quarter of a millennium earlier (Chladni, 1787). This also suggests  
614 that the dynamic of driven vacancy diffusion observed in the computer model reported  
615 here is a resonance feature of the pore and thus relates to diffusion eigenmodes. The  
616 resonance effect is less pronounced for gas diffusion (Fig. 7c) where the free paths  
617 between collisions can span the entire cell. Because the mass flow from relaxation site  
618 2 to the active site 3 can be sustained from any position at the pore wall the asymmetry  
619 parameter does not need to change sign when the active site moves along the pore  
620 wall (Fig. 7e), and the circular paths can have various shapes and can extend across  
621 the entire pore, so that the vortex pattern is largely washed out.

Given the technological importance of fluid motion in small pores in heterogeneous catalysis (Kärger et al., 2012), it will be interesting to explore, if such correlated motion resulting from standing longitudinal particle-concentration wave patterns near pore walls can be driven by external stimuli like ultrasound, electric or magnetic fields. The standing waves could be enhanced by tuning the driver frequency to the pore resonance like a musician enforces resonance modes on a flute when playing. To enhance the resonance modes, also low-power broad-band, forced oscillations can be considered such as in Fourier transform infrared spectroscopy (Michelson, 1903) and stochastic NMR spectroscopy (Ernst, 1970), while triggering free oscillations by high-power impulses may destroy the porous medium under study.

632



633

Figure 7. Illustration of the exchange asymmetry in driven equilibrium for the square pore of Fig. 6a. a) Depending on the sign of the asymmetry parameter, a small fraction of diffusing particles (blue circles) prefers the direct path towards or away from the active site (red square) at the pore boundary over the path along the boundary from the active site. b) Vacancy diffusion for negative asymmetry parameter and the active site 3 in the center of the pore wall. Jumps are limited to the next nearest cells. The direct path away from the active site to the bulk 1 in the center is preferred over the path along the pore wall 2 when leaving the contact region with the active site. c) Gas diffusion for negative asymmetry parameter and the active site 3 in the center of the pore wall. The free paths between collisions can span the entire cell. d) In-plane translational vacancy-diffusion paths resulting from the variation of the asymmetry parameters with the position of the active site on the pore wall depicted in Fig. 6g. e) Out-of-plane vibrational mode of a square plate observed by Chladni (Chladni, 1787).

647

648 **5. Summary**

649 The evidence provided by Monte Carlo simulations of random particle jumps on a 2D  
650 checkerboard and by simulations of 2D gas diffusion with topological confinements  
651 supports the notion, that asymmetry in three-site exchange maps reports the non-  
652 Brownian diffusion dynamics of confined particles in driven equilibrium. Depending on  
653 the sign of the asymmetry parameter, a small fraction of all particles prefers the direct  
654 path towards or away from the active site at the pore boundary over the path along the  
655 boundary to or from the active site resulting in a circular flux (Fig. 7). Both, driven  
656 vacancy diffusion and driven gas diffusion produce congruent results. These are:  
657 1) Circular exchange is a manifestation of driven equilibrium and leads to asymmetry  
658 of exchange peaks, while thermodynamic equilibrium manifests itself in detailed  
659 balance and symmetry of exchange peaks. 2) The circular exchange in driven  
660 equilibrium appears to be a resonance phenomenon which can potentially be driven  
661 by external stimuli. Yet, the reported simulations are limited to two dimensions, and it  
662 may be argued that the asymmetry of exchange vanishes in the more common pores  
663 with three spatial dimensions. But two-dimensional diffusion is not an abstract model  
664 and arises for gas atoms adsorbed to metal surfaces (Oura et al., 2013), so that the  
665 driven coherent particle diffusion indicated by the non-zero asymmetry parameter may  
666 be observed there. Given the congruent simulation evidence for driven vacancy  
667 diffusion and gas diffusion in two-dimensional confinements it is hypothesized, that  
668 confined diffusion can be partially converted to coherent motion by external excitation  
669 so that detailed balance will be violated as observed in nonequilibrium phenomena  
670 (Gnesotto et al. 2018, Lynn et al. 2021).

671

672 **Author Contributions**

673 BB posed the question, executed the simulations of confined vacancy diffusion, and  
674 wrote the manuscript. MA worked out the algorithm for vacancy diffusion along with  
675 BB and supervised MP. MP programmed the algorithm for confined gas diffusion and  
676 executed the gas-diffusion simulations.

677

678 **Acknowledgement**

679 BB thanks Thomas Wiegand at RWTH Aachen University for stimulating discussions,  
680 hosting him as a PostProf, and access to the computing facilities. He also thanks Ilya  
681 Kuprov for his flash of inspiration on linking three-site exchange to Fick's second law

682 at a random EUROMAR 2022 breakfast encounter and Stephan Appelt, Gerd  
683 Buntkowsky, Jeffrey Reimer, and Tom Barbara for stimulating discussions. Special  
684 thanks go to the unknown reviewer who commented on the manuscript (Gao and  
685 Blümich, 2020), that asymmetry in three-site exchange violates the principle of detailed  
686 balance and to the anonymous reviewer of this manuscript who educated the authors  
687 on the intricacies of Monte Carlo simulations.

688

### 689 **Code availability**

690 The codes for simulating confined 2D vacancy diffusion and confined 2D gas diffusion  
691 are reported in the supplement.

692

### 693 **Conflict of Interest statement**

694 Other than that BB is on the advisory board of Magnetic Resonance the authors  
695 declare no conflict of interest.

696

### 697 **References**

698 Bialynicki-Birula, I. and Bialynicky-Birula, I., *Modeling Reality*, Oxford University Press,  
699 Oxford, 2004.

700 Björgvinsdóttir, S., Moutzouri, P., Walder, B. J., Matthey, N., and Emsley, L.,  
701 Hyperpolarization transfer pathways in inorganic materials, *J. Magn. Reson.* 323,  
702 106888, 2021.

703 Brownstein, K.R. and Tarr, C. E., Spin-Lattice Relaxation in a System Governed by  
704 Diffusion, *J. Magn. Reson.* 26, 17–24, 1977.

705 Bunde, A., Caro, J., Kärger, J., and G. Vogel, eds., *Diffusive Spreading in Nature and*  
706 *Technology*, Springer Nature, Cham, 2018.

707 Bytchenkoff, D., and Rodts, S., Structure of the two-dimensional relaxation spectra  
708 seen within the eigenmode perturbation theory and the two-site exchange model, *J.*  
709 *Magn. Reson.* 208, 4–19, 2011.

710 Callaghan, P. T. and Stepišnik, J., Modulated Gradient NMR, *J. Magn. Reson.* 117,  
711 118–122 (1995).

712 Callaghan, P.T., *Translational Dynamics and Magnetic Resonance: Principles of*  
713 *Pulsed Gradient Spin Echo NMR*, Oxford University Press, Oxford, 2011.

714 Chladni, E. F. F., *Entdeckungen über die Theorie des Klanges*, Leipzig, Weidmanns  
715 Erben und Reich, 1787.

716 de Hoop, A.T. and Prange, M.D., Variational analysis of the natural decay rates and  
717 eigenmodes of cavity-enclosed diffusive fields, *J. Phys. A: Math. Theor.* 40, 12463–  
718 12477, 2007.

719 Einstein, A., Zur Quantentheorie der Strahlung, *Physikalische Zeitschrift* 18, 121–128,  
720 1917.

721 Ernst, R. R., Bodenhausen, G., and Wokaun, A., *Principles of Nuclear Magnetic  
722 Resonance in One and Two Dimensions*, ClarendonPress, Oxford, 1987.

723 Ernst, R. R., Magnetic Resonance with Stochastic Excitation, *J. Magn. Res.* 3, 10–27,  
724 1970.

725 Feynman, R., Leighton, R. B., and Sands, M., *The Feynman Lectures on Physics*, vol.  
726 1, chapter 46, Addison-Wesley, Reading, Fourth Printing, 1966

727 Fick, A., Ueber Diffusion, *Annalen der Physik* 94, 59–86, 1855.

728 Gao, Y., and Blümich, B., Analysis of three-site T<sub>2</sub>-T<sub>2</sub> exchange NMR, *J. Magn. Reson.*  
729 315, 106740, 2020.

730 Gnesotto, F. S., Mura, F., Gladrow, J., and Broedersz, C. P., Broken detailed balance  
731 and non-equilibrium dynamics in living systems: a review, *Rep. Prog. Phys.* 81,  
732 066601, 2018.

733 Grebenkov, D. S., A fast random walk algorithm for computing the pulsed-gradient  
734 spin-echo signal in multiscale porous media, *J. Magn. Reson.* 208, 243–255, 2011.

735 Grebenkov, D. S. and Nguyen, B.-T., Geometrical Structure of Laplacian  
736 Eigenfunctions, *SIAM Review* 55, 601–667, 2013.

737 Han, S.-I. and Blümich, B., Two-dimensional representation of position, velocity, and  
738 acceleration by PFG-NMR, *Appl. Magn. Res.* 18, 101–114, 2000.

739 Hughes, B. D., *Random Walks and Random Environments*, Clarendon Press, Oxford,  
740 1995.

741 Jeener, J., Meier, B. H., Bachmann, P., and Ernst, R. R., Investigation of exchange  
742 processes by two-dimensional NMR spectroscopy, *J. Chem. Phys.* 71 4546–4553,  
743 1979.

744 Kärger, J., Ruthven, D. M., and Theodorou, D. N., eds., *Diffusion in Nanoporous  
745 Materials*, vol. 1, Wiley-VCH, Weinheim, 2012.

746 Kundt, A., Über eine neue Art akustischer Staubfiguren und über die Anwendung  
747 derselben zur Bestimmung der Schallgeschwindigkeit in festen Körpern und Gasen,  
748 *Annal. Phys. Chem.* 203, 497–523, 1866.

749 Kuprov, I., private communication with BB at the EUROMAR 2022 conference in  
750 Utrecht, July 10–14, 2022.

751 Boltzmann, L., Weitere Studien über das Wärmegleichgewicht unter Gasmolekülen,  
752 Sitzungsber. Kais. Akad. Wiss., Wien, Math, Natruwiss. Classe 66, 275-370, 1872.

753 Lacabanne, D., Wiegand, T., Di Cesare, M., Orelle, C., Ernst, M., Jault, J.-M., Meier,  
754 B.H., and Böckmann, A., Solid-State NMR Reveals Asymmetric ATP Hydrolysis in the  
755 Multidrug ABC Transporter BmrA, *J. Am. Chem. Soc.* 144, 12431–12442, 2022.

756 Lee, J.-H., Labadie, C., Springer Jr., C. S., and Harbison G.S., Two-Dimensional  
757 Inverse Laplace Transform NMR: Altered Relaxation Times Allow Detection of  
758 Exchange Correlation, *J. Am. Chem. Soc.* 115, 7761–7764, 1993.

759 Lynn, C. W., Cornblath, W. J., Papadopoulos, L., Bertolero, M. A., and Bassett, D. S.,  
760 Broken detailed balance and entropy production in the human brain, *PNAS* 118,  
761 e2109889118, 2021.

762 Maxwell, J. C., On the dynamical theory of gases, *Philos. Trans. R. Soc. London* 157  
763 49–88, 1867.

764 McDonald, P. J., Korb, J.-P., Mitchell, J., and Monteilhet, L., Surface relaxation and  
765 chemical exchange in hydrating cement pastes: A two-dimensional NMR relaxation  
766 study, *Phys. Rev. E* 72, 011409, 2005.

767 Metropolis, N., Rosenbluth, A.W., Rosenbluth, M.N., Teller, A.H., and Teller, E.,  
768 Equation of State Calculations by Fast Computing Machines, *J. Chem. Phys.* 21,  
769 1087–1092, 1953.

770 Michel, M., Kapfer S. C., and Krauth, W., Generalized event-chain Monte-Carlo:  
771 Constructing rejection-free global-balance algorithms from infinitesimal steps, *J.*  
772 *Chem. Phys.* 140 054116, 2014.

773 Michelson, A. A., *Light Waves and Their Uses*, The University of Chicago Press,  
774 Chicago, 1903.

775 Müller, N. and Jerschow, A., Nuclear Spin Noise Imaging, *PNAS* 103, 6790–6792,  
776 2005.

777 Olaru, A. M., Kowalski, J., Sethi, V., and Blümich, B., Exchange relaxometry of flow at  
778 small Péclet numbers in a glass bead pack, *J. Magn. Reson.* 220, 32–44, 2012.

779 Onsager, L., Reciprocal Relations in Irreversible Processes, *Phys. Rev.* 37, 405-426,  
780 1931.

781 Oura, K., Lifshits, V. G., Saranin, A. A., Zotov, A. V., and Katayama, M., *Surface*  
782 *Science: An Introduction*, Springer, Berlin, 2013, chapter 13.

783 Parsons, E. C., Does, M. D., and Gore J.C., Temporal Diffusion Spectroscopy: Theory  
784 and Implementation in Restricted Systems Using Oscillating Gradients, *Magn. Reson.*  
785 *Med.* 55, 75–84, 2006.

786 Reviewer 2023, anonymous reviewer of Blümich, B., Parziale, M., and Augustine, M.,  
787 Monte-Carlo Analysis of Asymmetry in Three-Site Relaxation Exchange: Probing  
788 Detailed Balance, *Magnetic Resonance Preprint*, 2023, doi.org/10.5194/mr-2023-8.

789 Sabelfeld, K. K., *Monte Carlo Methods in Boundary Value Problems*, Springer-Verlag,  
790 Berlin, 1991.

791 Sandstrom, J., *Dynamic NMR Spectroscopy*, Academic Press, Cambridge, MA, 1983

792 Schlagnitweit, J. and Müller, N., The first observation of Carbon-13 spin noise spectra,  
793 *J. Magn. Reson.* 224, 78–81, 2012.

794 Seitz, F., On the Theory of Vacancy Diffusion in Alloys, *Phys. Rev.* 74, 1513–1523,  
795 1948.

796 Sleator, T., Hahn, E.L., Hilbert, C., and Clarke, J., Nuclear Spin Noise, *Phys. Rev. Lett.*  
797 55, 1742–1745, 1985.

798 Song, Y. Q., Detection of the High Eigenmodes of Spin Diffusion in Porous Media,  
799 *Phys. Rev. Lett.* 85, 3887–3881, 2000.

800 Song, Y.-Q., Venkataraman, L., Hürlimann, M. D., Flaum, M., Frulla, P., and Straley,  
801 C.,  $T_1$ - $T_2$  Correlation Spectra Obtained by Using a Fast Two-Dimensional Laplace  
802 Inversion, *J. Magn. Reson.* 154, 261–268, 2002.

803 Stepišnik, J., Mohoric, A., Lahajnar, G., Mattea, C., Stapf, S., and Sersa, I., Velocity  
804 autocorrelation spectra in molten polymers measured by NMR modulated gradient  
805 spin-echo, *Europhysics Lett.* 106, 27007, 2014.

806 Torrey, H. C., Bloch Equations with Diffusion Terms, *Phys. Rev.* 104, 563–565, 1956.

807 Valiullin, R., ed., *Diffusion NMR of Confined Systems*, R. Soc. Chem., Cambridge,  
808 2017.

809 van Kampen, N. G., *Stochastic Processes in Physics and Chemistry*, Elsevier,  
810 Amsterdam, 1992.

811 Van Landeghem, M., Haber, A., d’Espinose de Lacaillerie J.-B., and Blümich, B.,  
812 Analysis of Multisite 2D Relaxation Exchange NMR, *Concepts Magn. Reson.* 36A,  
813 153–169, 2010.

814 Wolf-Gladrow, D. A., *Lattice-Gas Cellular Automata and Lattice Boltzmann Models*,  
815 Springer, Berlin, 2000.